ELSEVIER

Materials Science and Engineering A266 (1999) 221–240

MATERIALS SCIENCE & ENGINEERING A

Three dimensional characterization and modeling of particle reinforced metal matrix composites part II: damage characterization

M. Li [a], S. Ghosh [a,*], O. Richmond [b], H. Weiland [b], T.N. Rouns [b]

[a] *Department of Aerospace Engineering, Applied Mechanics and Aviation, 209 Boyd Laboratory, The Ohio State University, 155 West Woodruff Avenue, Columbus, OH 43210, USA*
[b] *ALCOA Technical Center, Pittsburgh, PA 15069, USA*

Received 24 June 1998; received in revised form 16 November 1998

Abstract

This second paper of a two part sequence, attempts to quantitatively characterize 3-D microstructural damage in particle reinforced metal matrix composites using a combination of computational and experimental tools. It is perhaps the first studies providing quantitative 3-D characterization of phase and damage morphology for comparison with 2-D micrographs. Materials with different volume fractions and particle sizes, at different levels of deformation are considered. The serial sectioning method is used to obtain micrographs of a series of parallel sections of the sample material. 3-D computer images of the particles and the associated damage in the microstructure are constructed by digitally assembling the section micrographs. Equivalent microstructures with actual particles and cracks replaced by ellipses or ellipsoids are simulated for enhanced computational efficiency. The equivalent microstructures are meshed into Voronoi cells by a surface based algorithm. Various characterization functions of geometric parameters are generated to identify the damage size, shape, orientation and spatial distribution both in 2- and in 3-D. A sensitivity analysis is conducted to explore the influence of the morphological parameters on damage. Particle size, orientation and local volume fraction are found to play the most significant roles in the cracking process. Experimental observations of damage are compared with predictions by a probabilistic damage model viz. the Weibull model. Representative material elements, which correspond to the characteristic sizes for local continuum representation, are investigated through the use of variograms and marked correlation functions.

Keywords: Damage; Deformation; Microstructures; Morphology

1. Introduction

Interest in commercial use of particle-reinforced metal matrix composites (PRMMCs) in automotive, aerospace and other engineering systems has increased in the last few decades due to their potentially superior mechanical properties, as well as their ability to reduce life-cycle costs through enhanced thermal stability and weight reduction. Their cost-effectiveness in high volume production and the possibility of near-net shape processing by conventional metallurgical routes using existing equipment are added reasons for this interest. The property advantages of PRMMCs are, however, tempered by general degradation of properties like ductility and fracture toughness [1–7], which restrict their widespread use. Various experimental and numerical studies have been conducted to understand the influence of morphological factors such as volume fraction, size, shape and spatial distribution as well as constituent material and interface properties on the deformation and damage behavior. Embury and co-workers [8] have demonstrated that damage initiation is influenced by particle size, aspect ratio and spatial distribution. Zong et. al. [9] and Lewandowski et. al. [1,10–13] have investigated the evolution of damage measured in terms of reduction in tensile elastic modulus as well as change in Poisson ratio. Lewandowski et. al. [1–4,10–12,14–18] have also investigated the effect of matrix

* Corresponding author. Tel.: +1-614-2922599; fax: +1-614-2927369.
E-mail address: ghosh.s@osu.edu (S. Ghosh)

0921-5093/99/$ - see front matter
PII: S0921-5093(98)01133-2

microstructure, particle size, volume fraction spatial distribution and stress state on particle cracking, damage linkage and final failure of metal matrix composites. Llorca et. al. [19], Maire et. al. [20], Mummery et. al. [7] and Lewandowski et. al. [1–4,10–12,15–18] have experimentally shown the effect of morphology and matrix properties on reinforcement fracture and interfacial decohesion. Studies by Li and Ellyin [21] have revealed that the damage in alumina reinforced aluminum is primarily in the form of particle debonding and fracture as well as matrix cracking. Several numerical studies have also been conducted using probabilistic models e.g. the Weibull model, to relate particle fracture to strength, size and volume fraction with assumed particle shapes [5,8,22–25]. Nan and Clark [26] have used an effective medium approach to explore this dependence. Using the Voronoi cell finite element model, Ghosh and Moorthy [27,28] have examined the effect of various spatial dispersions and morphologies on the damage initiation and evolution process in ductile matrix composites. Pyrz and co-workers [29] have introduced novel descriptors to investigate the effects of different patterns on matrix and interface fracture by using truss like linkage models and unit cell methods. The above investigations conclude that predominant deformation induced damage mechanisms in PRMMC are matrix cracking, interface decohesion and reinforcement fracture. Characterization of the relation between microstructures and damage is a necessary ingredient for a complete understanding of the role of morphology on component life.

Experimental research with 2- and 3-D models [30] has revealed that damage assessment from 2-D sections can be very misleading, especially in the presence of spatial clustering. This subject has also been investigated by Lewandowski et. al. [15,18] and Lloyd [31] and referred to in [32]. It is necessary to examine the full 3-D characteristics for a comprehensive knowledge of the damage process. Most of the studies however are limited to 2-D sections of the material microstructure or their computer generated counterparts [34–38]. A few innovative stereological methods [39–42] and experimental techniques [43–45] have been pursued for obtaining 3-D microstructural information. These stereological methods are able to give only partial information on shapes, sizes and spatial distributions and are not effective in situations where detailed 3-D information is necessary. A few non-destructive evaluation methods have been proposed in recent years to detect damage. Among them are techniques based on ultrasonics e.g. [46,47] and methods of acoustic emission for monitoring damage [7,48,49]. Loss in modulus has also been used as an indirect measure of the damage level in [1,10–14,48,49]. While X-ray based computer topography (CT) [50,51] has emerged as a potential method for obtaining 3-D damage images, high resolution industrial CT systems are so far capable of achieving spatial resolutions only down to about 25 μm. Buffiere et al. [45] have developed a CT technology to yield topographic images with a high spatial resolution (≈ 6.5 μm X 6.5μm X 6.5 μm X).

This technique is however in a research stage and has not yet been commercialized. Most of the state of the art commercial 3-D experimental techniques cannot yield the necessary resolution (< 10 μm) for accurately capturing microscopic particles and damage.

Based on the serial sectioning method to obtain 3-D grain morphologies in polycrystalline materials by Weiland et. al. [52] and Li et. al. [33,30] have developed a technique to reconstruct 3-D PRMMC microstructures from serial sections. This method is inexpensive, yet highly accurate in the 1–3 μm range. As in the first part of this sequence [33], the serial sectioning method is used to obtain the 3-D microstructural parameters in this paper. Different classes of pre-strained Si particle reinforced aluminum matrix composites are analyzed. Material samples differ in particle volume fraction, particle size and deformation level. Computer simulated equivalent microstructures with elliptical or ellipsoidal particles and cracks are constructed for enhanced efficiency, which are followed by tessellation into meshes of 2- and 3-D Voronoi cells by a surface based algorithm. In Section 3, various characterization functions of geometric parameters are generated to identify the damage size, shape, orientation and spatial distribution. A sensitivity analysis is conducted in Section 4 to explore the influence of morphological parameters on damage. Experimental observations are compared with predictions by a probabilistic damage model viz. the Weibull model in Section 5. In Section 6, correlation and characteristic lengths are investigated through the use of variograms and marked correlation functions. Key factors which control the damage process in PRMMC materials are identified.

2. Material, microstructure and discretization

As mentioned in the first part of this two part sequence [33], the materials considered are 10 and 20% weight fraction composites of Al–Si–Mg alloy matrix with dispersed Si particles. Three material specimens are considered, viz. the 10BS with 10% weight fraction of smaller particles, 10BL with 10% weight fraction of larger particles, and 20BL with 20% weight fraction of larger particles. To induce different levels of microstructural damage by particle cracking, the specimens are uniaxially loaded to different strain levels at a constant strain rate [14,30]. Cylindrical tensile specimens with axes parallel to the extrusion direction and of nominal diameter 6.35 mm and gauge length 25.4 mm are prepared for this purpose. Tension tests are

executed at a crosshead speed of 0.042 mm s^{-1}. The samples considered are pre-strained to 1, 3, 4, 6 and 9% true strain.

To construct and visualize 3-D microstructures, a serial sectioning process is first used to generate a series of section micrographs, which are then serially stacked

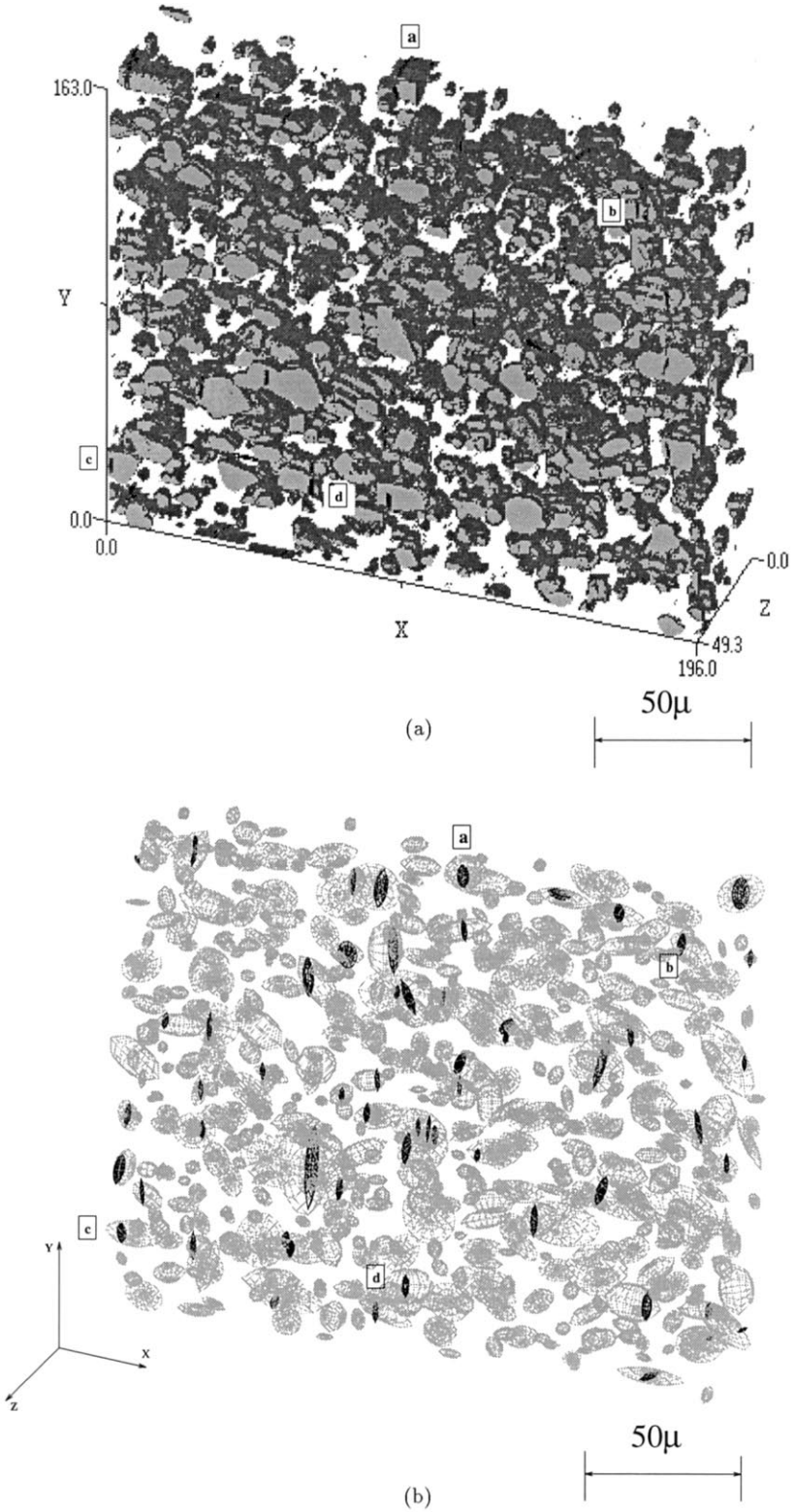

Fig. 1. 3-D microstructures of 10BL Al–Si–Mg composite: (a) A computer created image by serially arranging section micrographs. (b) Simulated microstructure of ellipsoidal particles and cracks (units in μm). A few cracks are identified with alphabets.

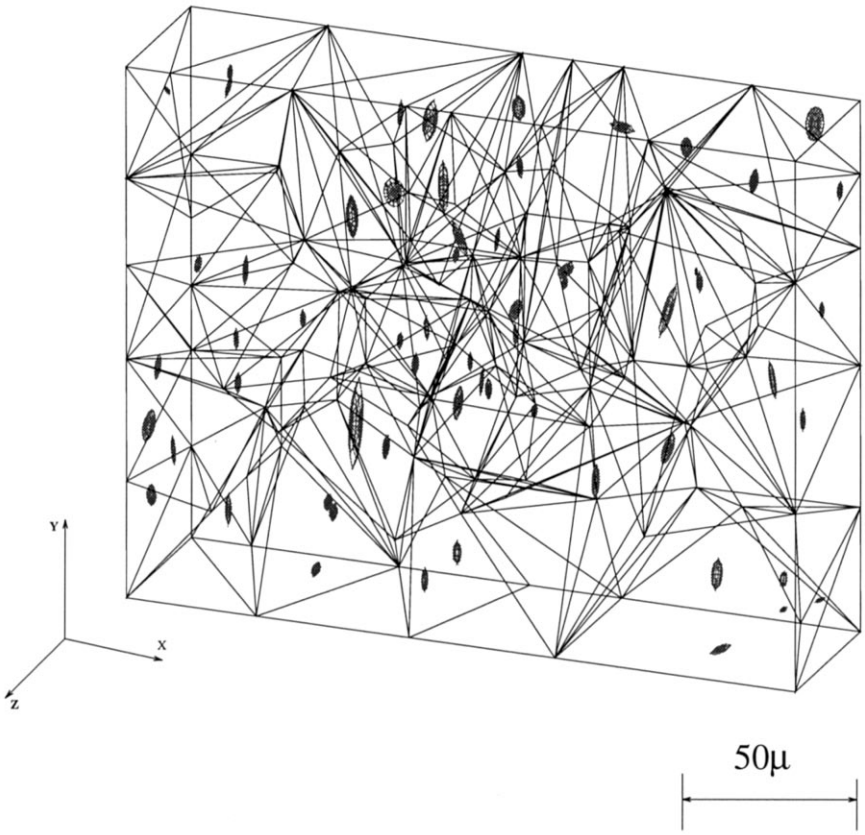

Fig. 2. 3-D Voroni tessellation of computer simulated microstructres generating a morphological mesh based on ellipsoidal micro-cracks for the 10BL Al–Si–Mg composite (units in μm).

on a computer for graphic analysis and viewing of 3-D volumetric data. The outcome of this process is shown in Fig. 1a for particles containing micro-cracks. To economize the image analysis and characterization process by way of well known geometric properties, equivalent microstructures are generated with each particle replaced by an ellipse (in 2-D) or an ellipsoid (in 3-D). The damage in the particles is in the form of micro-cracks with a finite separation between the crack faces. These crack openings are also simulated as equivalent ellipsoids. Digitized image data is first transferred into a binary format to distinguish between the crack, particle and matrix phases. The 0th (I_0), 1st (I_x, I_y) and 2nd (I_{xx}, I_{yy}) order geometric moments are then computed for each particle or crack, by adding contributions from each voxel (in 3-D) or pixel (in 2-D) that lies within the boundary of the heterogeneity. A computer simulated 3-D microstructure with equivalent particles (grey) and cracks (black) for the 10BL composite at 6% deformation is shown in Fig. 1b. The microstructures are then tessellated into a mesh of Voronoi cells, by an algorithm, based on (a) particle surface geometries [33] and (b) micro-crack surface geometries (Fig. 2b). Details of the microstructure reconstruction and tessellation procedures are discussed in [33,30]. Tessellation into a mesh of Voronoi cells plays an important role in developing geometric descriptors for quantitative characterization. They represent regions of immediate influence for each heterogeneity and also define neighboring regions by the cell facets. This facilitates easy evaluation of parameters like local area fractions, near neighbor and nearest neighbor distances and orientations.

3. Quantitative characterization of damage

The morphology of particle damage or micro-cracks can be characterized by various functions of orientation, shape, size and spatial distribution. A number of these classifier functions have been used to characterize various aspects of microstructural morphology in [33–37,29,14]. In this section, damage in the particles is represented by ellipsoids in 3-D as shown in part (b) of both Figs. 1 and 2, and as ellipses in 2-D. Then a few damage characterization functions for 3-D microstructures and their 2-D sections are presented. Results are presented for the 10BL composite at 1, 3, 6 and 9% strains, and for the 10BS and 20BL composites at 6% strain. The average values of all 2-D sections of the 10BL composites at 6% deformation are also provided.

3.1. Statistical parameters

3.1.1. Geometric features of damage

Tables 1 and 2 enumerate various statistical parameters reflecting the damage size, shape and spacing as seen in Figs. 1 and 2. The general number statistics for the damage with respect to particles are presented in Table 1. Specifically, they show: (i) the total number of particles (NP); (ii) the total number of micro-cracks (NC); (iii) the total number of multi-cracked particles (NMCP); (iv) the ratio of number of cracked particles to all particles (NFCP), and; (v) the ratio of volume of cracked particles to that for all particles (VFCP). There is a significant scatter in the total NP and the corresponding micro-cracks (NC) in the specimens considered. For the 10BL composite the NFCP increases steadily with strain. Also, this fraction is larger for the higher volume fraction 20BL than for the 10BL and 10BS composites at the same 6% strain. The NFCP and VFCP are all smaller for the 10BS microstructure with smaller particles than for the 10BL material. These results reveal the effect of the particle size on the damage intensity. The NMCP is also seen to increase significantly with volume fraction and deformation level. The mean 2-D observations are considerably different from the 3-D counterparts due to lack of cracks in a given section of the cracked particle.

In Table 2 some statistics of the geometric features of micro-cracks and their parent particles are given. In addition to ellipsoidal geometric features, viz. lengths and orientations of major, intermediate and minor axes, a size parameter is constructed through equivalent spheres (circles in 2-D). These spheres have the same volume as the ellipsoids and the diameter is obtained as:

$$\mathrm{EQS} = 2 \times \left(\frac{3}{4\pi} \times \mathrm{volume} \right)^{1/3} \text{ in 3D and EQS} = 2 \times \sqrt{\frac{\mathrm{area}}{\pi}} \text{ in 2D}$$

In the quantification of damage spacing, the nearest neighbor distance between micro-cracks is important. It is calculated as the minimum surface distance between a micro-crack and its neighbors that share common faces of the Voronoi cell in Fig. 2b. In Table 2: (i) MED, is the mean diameter of the equivalent cracks; (ii) MMIN, and; (iii) MMAJ, are the mean minor and major crack dimensions, respectively; (iv) MAR, is the mean damage aspect ratio expressed as the ratio of major axis to minor axis lengths; (v) MND, is the mean crack neighbor distance; (vi) RED, is the ratio of the mean equivalent diameter for cracked particles to that for all particles, and; (vii) RAR, is the ratio of the mean aspect ratio for cracked particles to that for all particles.

For the 10BL composite it is observed that the MED and MMAJ drop from high values at early stages of damage initiation as deformation increases. This is attributed to the fact that the larger particles are likely to crack first in the deformation process, yielding the largest mean damage size. This is consistent with experimental results reported in [1,2,10–12,16–18]. The smaller particles crack subsequently with smaller cracks and hence the mean value drops. It is interesting to note however that MAR consistently decreases and MMIN consequently increases with deformation, primarily due to the increasing separation between crack faces. As is expected, the smaller particles (10BS) have smaller damage size than the larger particles (10BL and 20BL). However the mean damage size in the 20BL is found to be smaller than in the 10BL. Also the equivalent size and major axis length in 3-D is larger than in 2-D since the sections may not contain the largest dimensions. An interesting observation is that MND between neighboring cracks follows the same trend as the mean size with increasing deformation, particle size and volume fraction. The RED decreases with deformation, while the RAR generally increases. The fact that RED is significantly greater than 1.0 indicates the importance of the size effect on particle cracking.

3.1.2. Relation with loading direction

Table 3 presents parameters portraying the orientation of particles with respect to the loading direction.

Table 1
Statistical parameters for damaged composite microstructures at various strains[a]

Material	Strain (%)	NP	NC	NMCP	NFCP	VFCP
10BL	1	624	0	0	0.0000	0.000
10BL	3	486	8	0	0.0165	0.137
10BL	6	596	61	5	0.0939	0.340
10BL	9	750	158	43	0.1533	0.470
10BS	6	1639	88	19	0.0421	0.195
20BL	6	727	238	79	0.2187	0.594
2-D-10BL	6	113	10	1	0.0866	0.255

[a] Abreviations: (NP) total number of particles, (NC) total number of micro-cracks, (NMCP) total number of multi-cracked particles, (NFCP) number fraction of cracked particles, (VFCP) volume fraction of cracked particles.

Table 2
Statistical parameters for damage in composite microstructures at various strains[a]

Material	Strain (%)	MED	MMIN	MMAJ	MAR	MND	RED	RAR
10BL	1	0.00 (0.00)	0.00 (0.00)	0.00 (0.00)	0.00 (0.00)	0.00 (0.00)	0.00	0.00
10BL	3	4.45 (0.90)	1.46 (0.48)	10.8 (3.54)	7.99 (3.55)	39.20 (17.45)	2.38	0.86
10BL	6	3.72 (1.60)	1.52 (0.59)	8.49 (4.82)	5.54 (2.01)	13.94 (7.98)	1.70	1.26
10BL	9	3.50 (1.40)	1.67 (0.59)	7.03 (3.65)	4.22 (1.66)	6.76 (4.93)	1.59	1.18
10BS	6	2.35 (0.90)	1.20 (0.38)	5.23 (3.34)	4.65 (3.87)	8.07 (6.75)	1.93	1.14
20BL	6	3.07 (1.36)	1.40 (0.53)	6.76 (4.10)	4.86 (2.60)	5.46 (4.09)	1.56	1.12
2D-10BL	6	2.95 (1.16)	1.51 (0.45)	5.88 (3.79)	3.87 (1.97)	31.77 (18.58)	1.91	1.16

[a] Abreviations used: (MED) mean of equivalent crack diameter, (MMIN) mean of crack minor axis length, (MMAJ) mean of crack major axis length, (MAR) mean of crack aspect ratio, (MND) mean of crack nearest neighbor distance, (RED) ratio of the mean equivalent diameter for cracked particles to that for all particles, (RAR) ratio of the mean aspect ratio for cracked particles to that for all particles, (in μm). Numbers in parenthesis represent corresponding standard deviations.

This orientation plays an important role in particle fracture. The parameters are: (i) the mean projection of cracked particle cross-sectional area perpendicular to the loading direction (MCPTA); (ii) the ratio of the mean projected cross-sectional area for cracked particles to all particles (RTA); (iii) the mean projection of the cracked particle major axis along the loading direction (MCPDL); (iv) the ratio of the mean major axis projection along the loading direction for cracked particles to all particles (RDL); (v) the mean cross-sectional area obtained by projecting the crack perpendicular to the loading direction (MCTA), and; (vi) the mean projection of crack major axis along the loading direction (MCDL). The projected cross-sectional area perpendicular to the loading direction corresponds to the largest transverse area in this direction. The fact that RTA is significantly larger than 1.0 implies that particles with larger transverse cross-sectional areas are likely be cracked. Both MCPTA and RTA decrease with increasing strain, as do MCPDL and RDL, again demonstrating cracking of larger particles first. The projected crack length MCDL increases with deformation while the transverse area decreases due to cracking of smaller particles. A comparison of MCTA and MCPTA shows that MCTA is less than the corresponding MCPTA, implying that not all damage occurs at the centers of the particles and may not completely split the particles.

3.1.3. Statistics of multiple cracked particles

Some statistics of particle multiple cracking are provided in Table 4. These are: (i) the mean of cracked particle volumes (MCPV); (ii) the mean of multiply cracked particle volumes (MMCPV); (iii) mean cracked particle length (MCPL); (iv) mean multi-cracked particle length (MMCPL); (v) mean cracked particle aspect ratio (MCPAR), and; (vi) mean multi-cracked particle aspect ratio (MMCPAR). The generally higher volumes and lengths of multiply cracked particles are reflected in MMCPV and MMCPL being larger than MCPV and MCPL, respectively. These volumes and lengths consistently increase with deformation. The deformation effect is less pronounced for parameters related to aspect ratio viz. MCPAR and MMCPAR. However, it is noticed that particles with higher aspect ratio are likely to have more cracks (MMCPAR > MCPAR). To sum up, large particles with high aspect ratio and orientations closer to the loading direction are most prone to multi-cracking.

3.2. Statistical functions of damage orientation and shape

The direction of overall loading is a determining factor in the orientation of particle damage. In Fig. 3, a histogram of the cumulative damage lengths as a function of angular position with respect to the loading direction x and the two perpendicular directions y and z, are plotted. The cumulative length in a given direction is calculated as the sum of the projected major axis length in that direction. Plots are for the 10BL composite at 6% strain. It can be seen that there is a preponderance of cracks at right angles to the loading direction x. Another effective means of characterizing shapes is the form factor discussed in [33,35]. This dimensionless factor is unity for a perfect circle (2-D) or sphere (3-D) and decreases in value with increasing shape irregularity. Both 2- and 3-D form factors are plotted as functions of equivalent size (diameter) in Fig. 4a and b. The form factor steadily decreases with increasing crack size, suggesting that larger cracks have higher degrees of shape irregularity. This is different from the effect of particle form factors described in [33], where size does not have a strong influence. Also the 3-D slope is significantly less than that for 2-D sections. An alternate measure of shape distributions is depicted through the probability density functions $f(AR)$ of aspect ratio in Fig. 4c and d. Fig. 4c shows these functions with increasing deformation levels while Fig. 4d is for different materials. The peaks in $f(AR)$ occur

at lower aspect ratio with increasing deformation. Consistent with observations in Table 2, these peaks occur at larger aspect ratio for the 10BL than for the 10BS and 20BL composites. Peaks for 2-D sections are higher than those for 3-D.

3.3. Statistical functions of damage size and spacing

The cumulative distribution functions of the equivalent damage size $F(d)$ and the major axis length $F(ml)$ are plotted in Fig. 5a and b, respectively. Higher gradients in F (and consequently higher peaks in the probability density) at lower values of damage size and length are observed for the 10BS and 20BL materials. For the 10BL composite at 3% strain, the distribution functions begin at a higher crack size and have a very high gradient. This indicates that at this strain only the larger particles crack, yielding large damage size. With increased straining, the starting value of F decreases to accommodate smaller cracks. The larger plateaus in F are the result of the lack of additional cracking with continued deformation. Cumulative distribution functions and probability density functions of the surface to surface nearest neighbor distances ($F(d_{NN}), f(d_{NN})$) are plotted in Fig. 6a and b. The nearest neighbor distance (d_{NN}) is computed as the smallest distance between neighboring damage sites, where neighbors share common edges of a Voronoi cell as illustrated in Fig. 2b. With increasing deformation level or particle volume fraction, peaks in ($F(d_{NN})$ are higher but occur at lower values. In contrast, lower peaks at larger values of d_{NN} occur with increasing size.

4. Sensitivity of damage to morphology

It is clear from the above study that damage related to particle cracking depends on such local morphological variables as volume fraction, size, shape, orientation and spatial distribution of the particles as well as the constituent material and interface properties and applied loads. For their incorporation in a damage model, a sensitivity analysis would measure how sensitive a damage parameter is with respect to these morphological variables and provide gradient information to be used in the model construction. While formulating a damage model is beyond the scope of this study, a sensitivity analysis is done to motivate such a model. Two damage parameters, viz. the NFCP and the VFCP are used to manifest the damage level in the composite. The sensitivity studies are done with the 10BL material at 6% strain. In Figs. 7 and 8, the dots correspond to the actual data obtained for the sample. A linear interpolation obtained by a least square fit yields the corresponding overall gradient or slope. The abscissae are normalized with respect to the maximum values to provide a unit scale.

4.1. Particle size

Both plots of NFCP and VFCP as functions of the equivalent particle size in part (a) of both Figs. 7 and 8 show similar variations. The steep slopes correspond to the significance of the effect that this variable has on damage. The unit values of NFCP and VFCP at higher values of size indicate that all particles in this size range are cracked. With increasing strain, there is a shift in these plots to the left, implying the cracking of smaller particles. The slope also increases slightly, showing that the size effect is even more pronounced with evolving deformation.

4.2. Particle shape

The slope for NFCP as a function of particle aspect ratio in Fig. 7b is considerably larger than that for VFCP in Fig. 8b. Both of them are however lower than that for size, implying a relatively diminished effect of shape. However, there is a much larger scatter in the data for shape, probably due to lack of a well defined functional dependence.

Table 3
Statistics of particle cracking with respect to the loading direction (LD)[a]

Material	Strain (%)	MCPTA	RTA	MCPDL	RDL	MCTA	MCDL
10BL	3	137.97	4.374	15.57	2.236	40.46	1.49
10BL	6	72.00	2.397	13.73	1.894	22.23	1.59
10BL	9	52.79	2.105	12.80	1.722	18.14	1.77
10BS	6	34.56	3.020	8.18	1.925	6.78	1.39
20BL	6	58.14	2 045	1.94	1.633	14.52	1.56

[a] Abreviations: (MCPTA) mean cracked particle maximum transverse cross-sectional area perpendicular to (LD) in μm^2, (RTA) the ratio of the mean maximum transverse cross-sectional area perpendicular to (LD), for cracked particles to all particles, (MCPDL) mean projection of the cracked particle major axis along (LD) in μm, (RDL) ratio of the mean projection of major axis along (LD), for cracked particles to all particles, (MCTA) mean of maximum transverse crack cross-sectional area, perpendicular to (LD) in μm^2 and (MCDL) mean projection of crack major axis along (LD) in μm.

Table 4
Statistics of multiply cracked particles[a]

Material	Strain (%)	MCPV	MMCPV	MCPL	MMCPL	MCPAR	MMCPAR
10BL	3	1790.3	–	23.23	–	2.280	–
10BL	6	810.1	989.0	18.34	18.80	3.138	2.91
10BL	9	571.0	1149.4	16.13	22.91	3.046	3.72
10BS	6	243.1	276.2	12.42	13.83	3.055	3.29
20BL	6	590.3	915.9	16.41	20.33	3.209	3.49

[a] Abreviations: (MCPV) mean cracked particle volume in μm^3, (MMCPV) mean multi-cracked particle volume in μm^3, (MCPL) mean cracked particle length in μm, (MMCPL) mean multi-cracked particle length in μm, (MCPAR) mean cracked particle aspect ratio, (MMCPAR) mean multi-cracked particle aspect ratio.

4.3. Particle orientation

Particle orientation with respect to the loading direction is indirectly represented by the maximum cross-sectional area projected perpendicular to the loading direction. It is indicative of the size as well as orientation. The fractured particle fractions as a function of this transverse area are plotted in part (c) of both Figs. 7 and 8. Once again, a high value of the slope for NFCP and VFCP, represents a strong effect of the size at a particular orientation with respect to the loading direction.

4.4. Local volume fraction

The local volume fraction is measured as a ratio of particle size to the volume of the associated Voronoi cell. The local volume fraction is effective in distinguishing between spatial distributions, especially with respect to clustering. A higher fraction implies a local region rich in particles and consequently clustering. In part (d) of both Figs. 7 and 8, the number and volume fraction of cracked particles increases rapidly with local volume fraction and the slope is quite high. The strong influence of clustering in particle rich regions on particle cracking is clearly illustrated by this result.

4.5. Nearest neighbor distance

A particle is a neighbor of another particle if their Voronoi cells share a common edge. The nearest neighbor correspond to neighbors with the minimum surface separation distance. While mean neighbor distance can effectively classify clustering, the nearest neighbor distance may not necessarily be a good indicator of spatial distribution. The fraction of cracked particles are plotted as functions of the inverse of the nearest neighbor distance in part (e) of both Figs. 7 and 8. While the trend is still the same as the other parameters, a weak influence on particle cracking is manifested by a small slope. This shows that a single or fewer neighboring particles may have a reduced effect on damage.

4.6. Nearest neighbor orientation

The nearest neighbor orientation is measured as the angle between a line joining the centers of particle and its nearest neighbor, and the loading direction. It denotes the relative orientation of nearest neighbors in reference to the loading direction. Particle cracking as a function of the inverse of this orientation is plotted in part (f) of both Figs. 7 and 8. While the NFCP plot projects a small slope, the slope for the VCFP plot is considerably higher. This shows that the propensity to crack decreases with increased angular position from the loading direction.

In summary, the sensitivity analysis infers that the strongest influence on particle cracking comes from the size, transverse section areas and local volume fraction reflecting spatial distribution. Particle shape and nearest neighbor distance show much less sensitivity to particle cracking. The influence of straining on the initiation and growth of overall damage in the microstructure is further studied by considering the primary (major axis) and secondary (minor axis) lengths of particle cracks. The primary length manifests the initiation (and immediate propagation) of cracks while the secondary length represents the crack surface separation due to matrix deformation. In the analysis, the crack dimensions are normalized with respect to equivalent particle size and the mean is calculated as:

$$MNL = \frac{\sum_{i=1}^{N_{cr}} \frac{l_i}{d_i}}{N_{cr}} \quad (1)$$

Here MNL corresponds to the mean primary or secondary crack dimension, l_i and d_i are the corresponding length and equivalent diameter, respectively for the ith cracked particle and N_{cr} is the total number of cracked particles. Fig. 9 illustrates the variation of the two principal lengths as a function of straining. Following a rapid increase at the early stages of deformation, the mean primary crack length plateaus off followed by a slight decline. This is due to larger particles cracking first and subsequently the smaller particles. The mean secondary length on the other hand steadily increases at

a considerably slower rate, implying a slower increase in crack face spacing by deformation. In modeling damage by particle cracking, a damage parameter D may thus be represented in a parametric form as:

$$D = D(p(v), p(o), g(r), S_m, S_p, \in) \quad (2)$$

where $p(v)$ is the size distribution, $p(o)$ *is* the orientation distribution of neighbors, $g(r)$ characterizes a spatial distribution function like radial or pair distribution functions, or probability density of local volume fraction [34,35], S_m, S_p are constituent material properties and $\in$ is the deformation level.

5. Comparisons with a probabilistic damage model

The two and three parameter Weibull models have been widely used in the literature [5,22,24,25] to make predictions on brittle particle failure in ductile matrix composites. These models are based on weakest link statistics in which the particle fails when a flaw size, in a random distribution of flaws, becomes critical. In the two parameter model, the cumulative probability of fracture F_{fr} for a particle of volume v subjected to an average tensile stress σ_p is given as:

$$F_{fr} = 1 - \exp\left[-\frac{v}{v_0}\left(\frac{\sigma_p}{\sigma_0}\right)^m \right] \quad (3)$$

where v_0 and σ_0 are reference volume and stress parameters, respectively and m is the Weibull modulus. For a known probability distribution of particle volumes in a microstructure $p(v)$, the fraction of fractured particles may be obtained as (see [22]):

$$\rho(V) = \int_{V_{min}}^{V_{max}} p(v) F_{fr}\, dv \qquad \text{(without shape effects)} \quad (4)$$

where $V_{min} \rightarrow V_{max}$ give the range of particle volumes. A modified formula results when the shape distribution of particles is considered in addition to volume distribution. If $p(\alpha)$ corresponds to the probability density function of aspect ratio α, the fraction of cracked particles suggested in [53] is given as:

$$\rho(\alpha_{min}, \alpha_{max}, V_{min}, V_{max}) = \int_{\alpha_{min}}^{\alpha_{max}} \int_{V_{min}}^{V_{max}} p(\alpha) p(v) F_{fr}\, dv$$

(with shape effects) (5)

where $\alpha_{min} \rightarrow \alpha_{max}$ give the range of the particle aspect ratios. Eq. (5) assumes that the probability densities $p(\alpha)$ and $p(v)$ are uncorrelated. The probability density functions $p(v)$ and $p(\alpha)$ for the 10BL composite at 6% strain are plotted in Fig. 10.

In implementation of the Weibull model, the average particle stress σ_p is first computed by the finite element analysis of a cubic unit cell with a single spherical particle, as shown in Fig. 10c. Various 2- and 3-D unit cell models using the finite element method have also been used for damage modeling in [5,19,22,54–59]. While such a unit cell assumption trivializes the particle spatial distribution to a uniform square diagonal pattern, it is nevertheless an efficient way of evaluating average stresses. This FEM model also ignores shape effects. The particle size is determined by equating the total volume fraction in the microstructure to that in the unit cell. For the 10BL and 10BS composites, the sizes are calculated to be $L = 100$ and $R = 57.6$, while for the 20BL composite, $L = 100$ and $R = 72.6$. Only

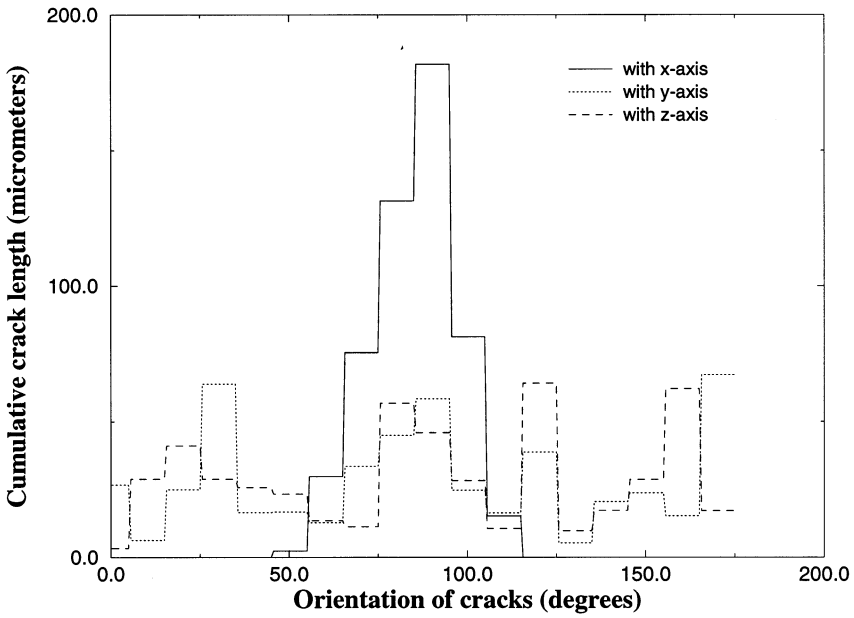

Fig. 3. Total damage length as a function of orientation for 10BL composite at 6% strain.

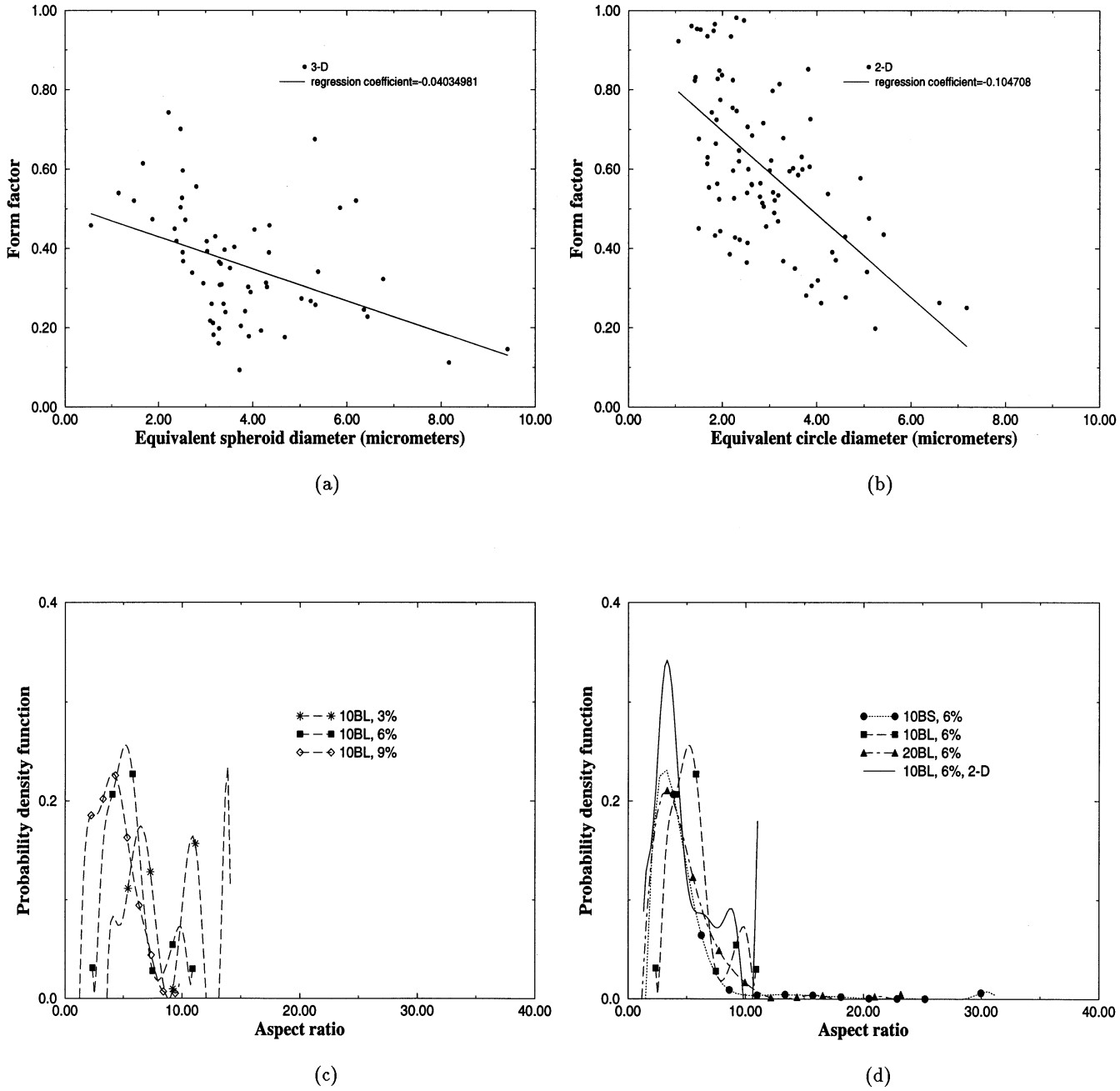

Fig. 4. Damage shape characterization: form factor as a function of equivalent crack size (diameter) for 10BS at 6% strain for: (a) 3-D; (b) average of 2-D sections; the probability density function of an aspect ratio for; (c) different deformation levels and; (d) for different materials.

1/8 of the unit cell is discretized into ten-node quadratic tetrahedron elements for FEM analysis by ABAQUS [60]. The resulting number of elements for the 20BL composite is 2499, while that for the 10BL/BS composites is 1966. The boundary conditions imposed include symmetry conditions, applied displacement conditions on $y = L$, and periodicity conditions on faces of the unit cell in Fig. 10c.

$$u_x = 0 \ \ on \ \ x = 0, \quad u_y = 0 \ \ on \ \ y = 0, \quad u_z = 0 \ \ on \ \ z = L$$

$$u_y = D \ \ on \ \ y = L \quad u_x = D_x^* \ \ on \ \ x = L,$$

$$u_z = D_z^* \ \ on \ \ z = 0$$

$$T_y = T_z = 0 \ \ on \ \ x = 0/L, \quad T_x = T_z = 0 \ \ on \ \ y = 0/L,$$

$$T_x = T_y = 0 \ \ on \ \ z = 0/L, \tag{6}$$

where u and T are the edge displacements and tractions, respectively. Periodicity is enforced on faces $x = L$ and $z = 0$ by requiring them to remain straight and parallel to the original direction throughout deformation. The corresponding displacements D_x^* and D_z^* are determined from the average force conditions:

$$\int_y \int_z T_x \, dy \, dz = 0 \text{ on } x = L,$$

$$\int_x \int_y T_z \, dy \, dz = 0 \text{ on } z = 0 \quad (7)$$

where T_x and T_z are the normal tractions on the surfaces. Material properties for the constituents are discussed in [14]. The Si particles are assumed to be linearly elastic with $E_p = 168$ GPa and $v_p = 0.17$. The Al–Si–Mg matrix is modeled as an isotropically hardening elastic-plastic solid with elastic coefficients $E_m = 71$ GPa and $v_m = 0.33$. The flow stress in plasticity is determined from the equivalent stress–strain curve (plotted in Ref. [61]). Then the average tensile (y-direction) stress in the particle is calculated by averaging this stress over all the elements contained within the particle as:

$$\sigma_p = \frac{\sum_{e=1}^{N_p} \int_{Ve} \sigma_{yy} \, dv}{\sum_{e=1}^{N_p} \int_{V_e} dv} \quad (8)$$

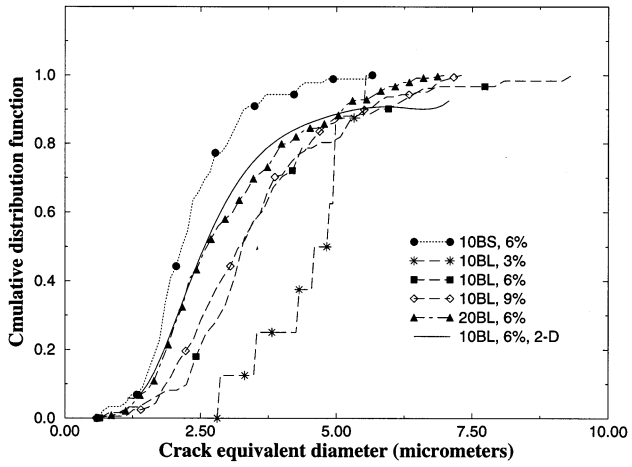

(a)

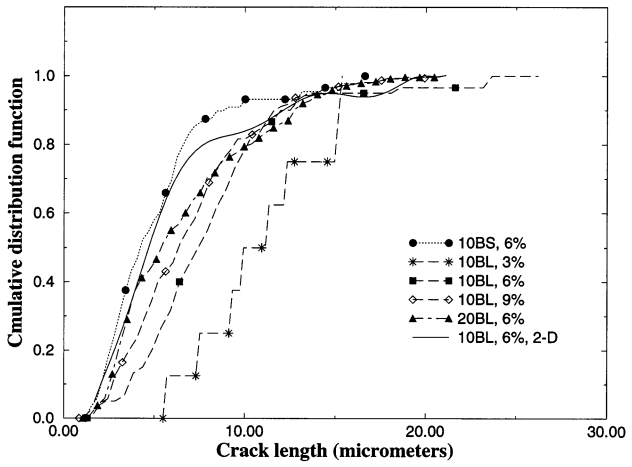

(b)

Fig. 5. Cumulative distribution function of: (a) equivalent crack size (diameter), and; (b) crack major axis length.

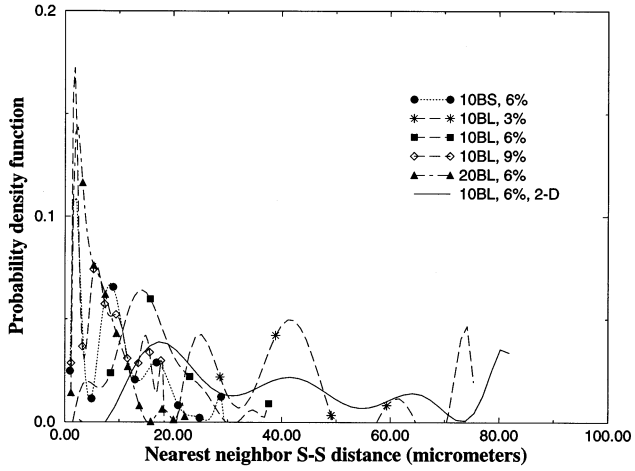

(a)

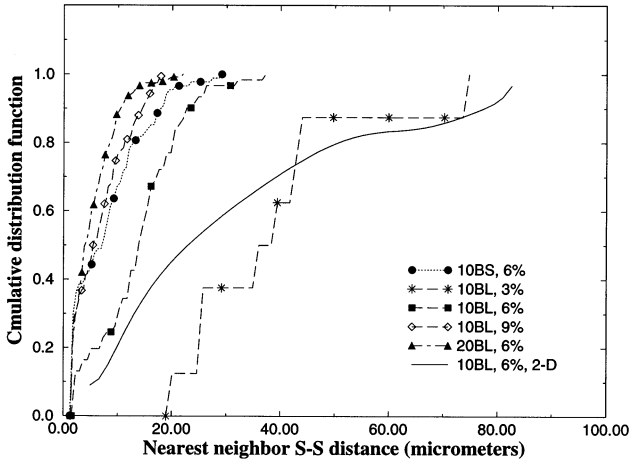

(b)

Fig. 6. (a) Probability density function and (b) cumulative distribution function, of a crack surface neasrest neighbor distance.

where V_e is the volume of eth element, σ_{yy} is the tensile stress in the element and N_p is the total number of elements in the particle. The element stresses are calculated at integration points and integrated by Gaussian quadrature.

Calibration of the parameters m, v_0 and σ_0 in the Weibull model are done with results for the 10BL composite at 6% deformation. This sample microstructure has an average particle volume of $\bar{v} = 223.5$ μm^3 and a cracked particle fraction of $\rho = 9.39\%$. The average particle stress is obtained from ABAQUS simulation as $\sigma_p = 422.54$ MPa. The Weibull parameter m in various studies e.g. [25,53] is assumed to vary as integers between 1 and 8. Accordingly, the same variation is tested in this work. The reference volume v_0 is taken as the average particle volume $\bar{v}$. Both Eqs. (4) and (5) without and with shape effects are considered for calibrating σ_0. The integrals in Eqs. (4) and (5) are evaluated numerically, where the probability density functions $p(v)$ and $p(\alpha)$ are measured from the graphs

in Fig. 10a and b. The steepest descent method is used to solve for the resulting nonlinear solution. Results of this calibration are documented in Table 5. Larger variations in σ_0 are noted for smaller values (1–4) of m.

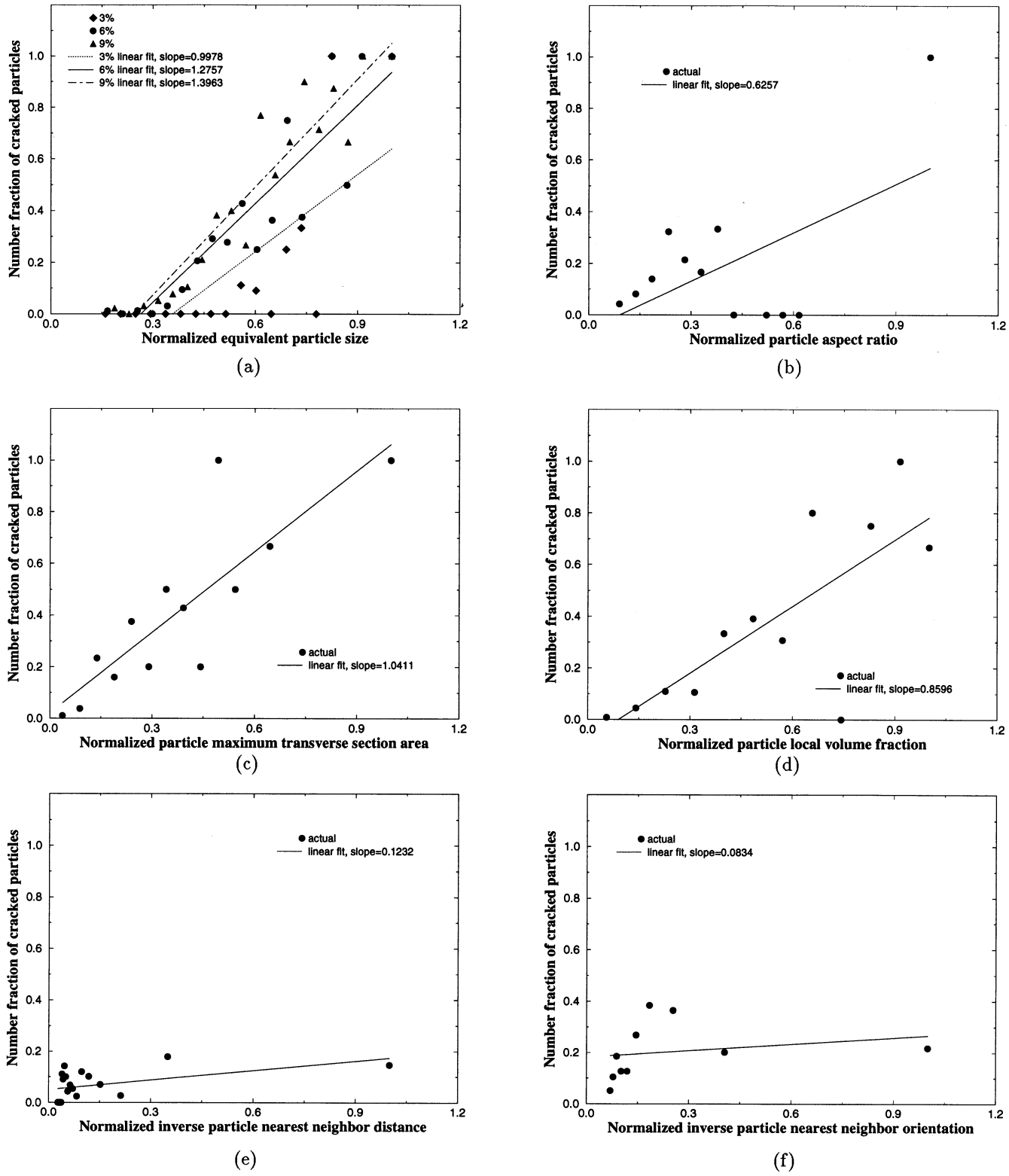

Fig. 7. Sensitivity analysis with number fraction of cracked particles vs. (a) equivalent particle size; (b) particle aspect ratio; (c) cross sectional area perpendicular to the loading direction; (d) particle local volume fraction; (e) particle nearest neighbor distance; (f) particle nearest neighbor orientation with respect to the loading direction.

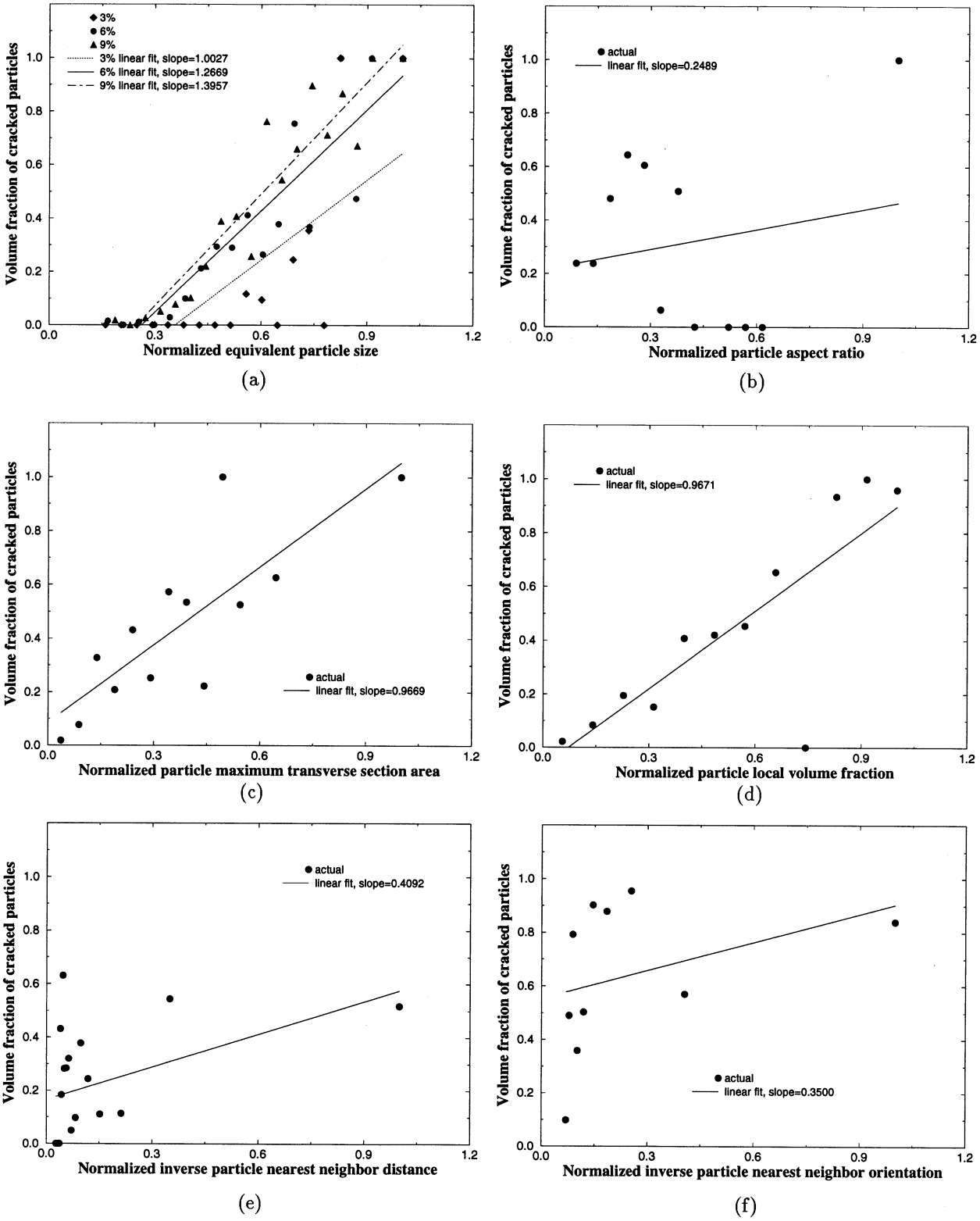

Fig. 8. Sensitivity analysis with volume fraction of cracked particles vs. (a) equivalent particle size; (b) particle aspect ratio; (c) cross sectional area perpendicular to the loading direction; (d) particle local volume fraction; (e) particle nearest neighbor distance; (f) particle nearest neighbor orientation with respect to the loading direction.

With these calibrated parameters, the fraction of cracked particles in the 10BL composite at 9% strain, the 20BL composite at 6% strain and the 10BS composite at 6% strain are subsequently predicted by the

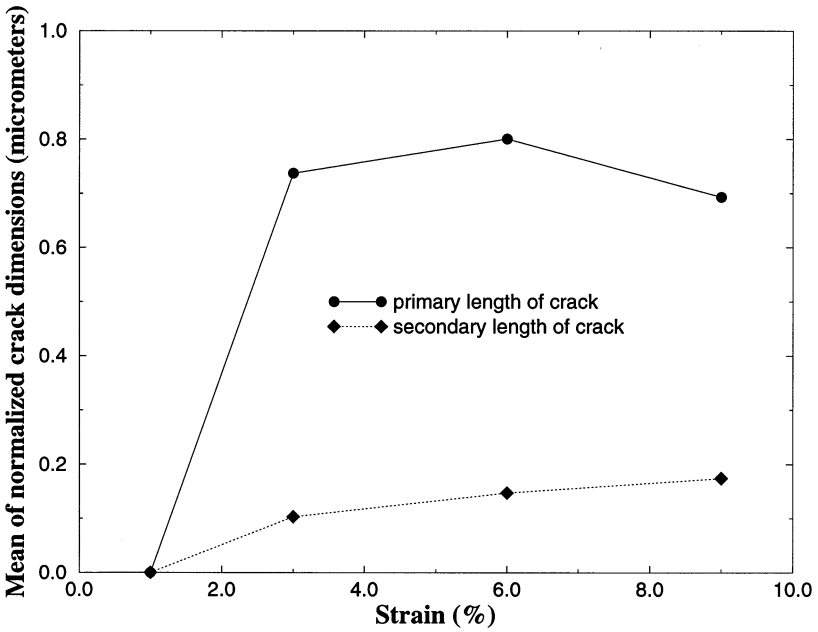

Fig. 9. Damage size evolution as a function of straining.

Weibull model. Results are shown in Table 6. Pertinent variables in the Weibull model for these materials are:

10BL composite at 9% strain: $\rho = 15.33\%$, $\sigma_p =$ 471.08 MPa and $\bar{v} = 186.4\ \mu m^3$

20BL composite at 6% strain: $\rho = 21.87\%$, $\sigma_p =$ 484.01 MPa and $\bar{v} = 217.41\ \mu m^3$

10BS composite at 6% strain: $\rho = 4.21\%$, $\sigma_p = 422.54$ MPa and $\bar{v} = 52.4\ \mu m^3$

For the 10BL composite at 9% strain, best concurrence with the experimentally observed results is achieved with (i) $m = 5 \sim 6$ without shape effects and (ii), $m = 7 \sim 8$ with shape effects. For the 20BL composite best results are obtained with $m = 7$ without shape effects. Predictions do not match the observed results for the given range of m when shape effects are considered. Similar observations are also made with the 10BS composite. From these results it may be inferred that the Weibull model is effective in predicting the extent of damage for some microstructures, but it has some drawbacks. It is likely that the procedure for incorporating shape effects, that have relatively smaller effects as seen in the sensitivity analysis, is not appropriate. Besides, this model does not account for particle orientation and spatial distributions, which are significant. It is therefore effective in only a few select cases where these effects are not appreciable.

6. Characteristic size of microstructures

The influence region of local morphology on thermo-mechanical response is characterized by a microstructural representative material element (RME) that is critical in determining length scales. The RME depicts a region which is assumed to be representative of the entire microstructure. Local distributions of stresses, strains and damage are sensitive to perturbations in local morphology and, consequently, functions that distinguish between their variations for different microstructural patterns can provide insight into microstructure-property relations. In this section, two measures are estimated for the size of the microstructural RME. The first is based on the construction of variograms as described in [62], while the second is based on marked correlation functions discussed in [38,28,35].

6.1. Variograms and correlation length

Following approaches in geostatistics, any observed variability may be analyzed by means of a second order moment. Consequently, a variogram $\gamma(h)$ *is* defined as one half of the variance of the difference in the paired values of a characterizing variable X, that are separated by a distance h. In this work, the variogram function $\gamma(h)$ is expressed as:

$$\gamma(h) = \frac{1}{2N(h)} \sum_{i=1}^{N(h)} [X(x_i + h) - X(x_i)]^2 \quad (9)$$

The characterizing function X depends on the microstructure and takes values 0 or 1. It corresponds to

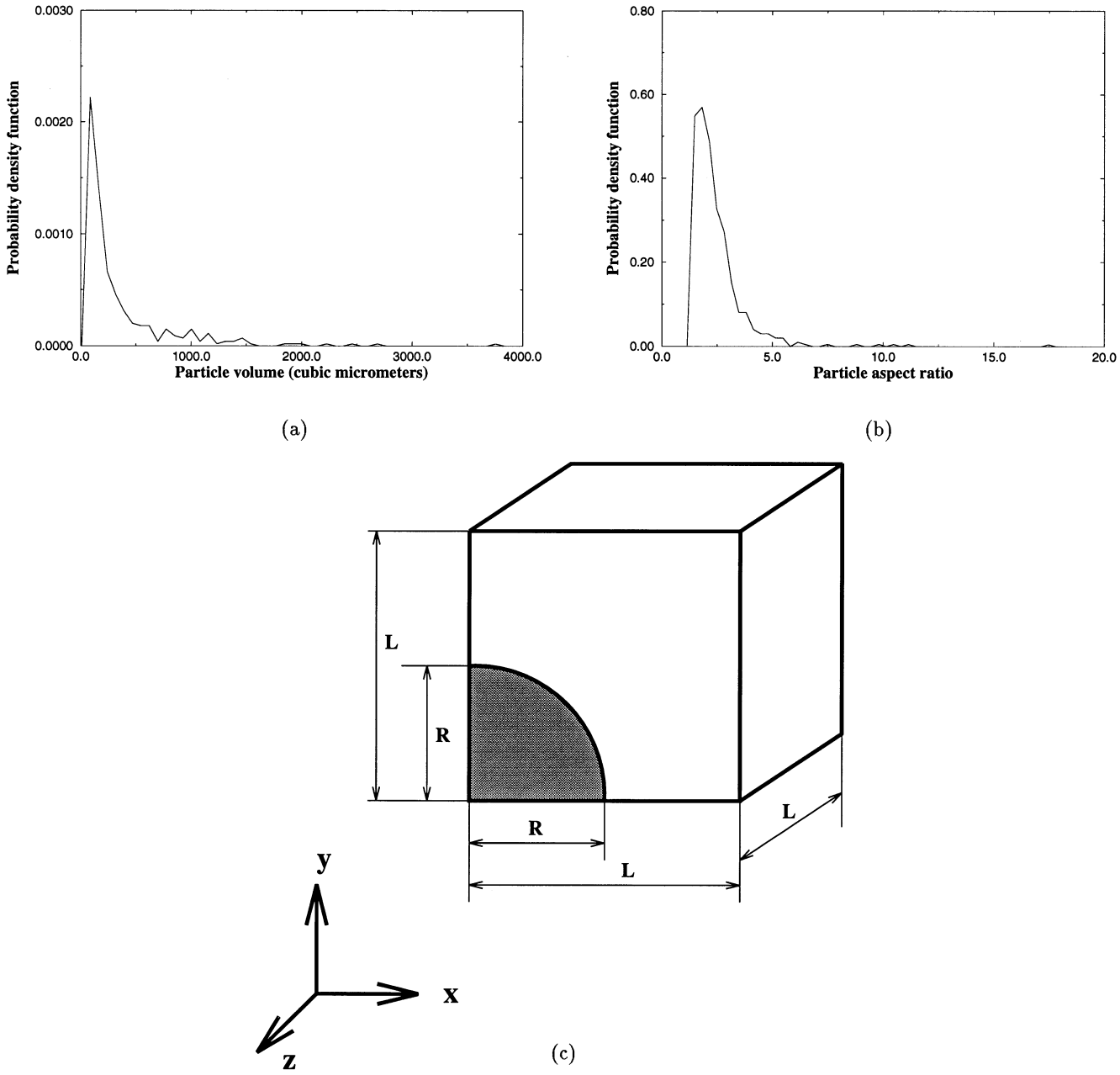

Fig. 10. Weibull model data for 10BL composite at 6% probability density function: (a) of particle volume; (b) of particle aspect ratio; (c) 1/8 of the unit cell used in FEM analysis for particle stress.

the volume element or voxel information of digitized microstructural images stored in a binary format. If a voxel at a specified coordinate x lies within a particle (grey/black), X is assigned a value 0. If the voxel lies in the matrix (white), X takes a value 1. $N(h)$ corresponds to the total number of voxels in a certain direction with a given separation value of h, and $[X(x_i+h)-X(x_i)]$ has a value 0 or 1 depending upon the location of points in the pair. Such a variogram can be used in the evaluation of correlation lengths in an autocorrelation function.

Variograms of 10BL material at 9% deformation are plotted for the x-(loading direction), y- and z-directions in Fig. 11. For this material, the microstructural element has dimensions 196 μm × 163 μm × 48.41 × μm. The h in Eq. (9) along a certain direction is taken to be less than or equal to half of the corresponding microstructural dimension. In Fig. 11a the variogram is for all particles, while it represents cracked particles only, Fig. 1b. Stability is assumed to be achieved when the fluctuations in $\gamma(h)$ are within a certain percent (7.5% in this study) of the maximum value. Both of the variograms stabilize and exhibit statistical independence with increasing h. The correlation length is estimated as

Table 5
Calibrated reference stress (MPa) for various m values, with results from 10BL composite at 6% strain

m	1	2	3	4	5	6	7	8
σ_0 Eq. (8)	2796	1088	794	678	617	5580	554	536
σ_0 Eq. (9)	739 560	17 689	5096	2736	1883	1468	2129	1076

the distance beyond which the variograms stabilize. Estimates are calculated for a number of material samples and tabulated in Table 7. The blanks correspond to cases where the variograms do not stabilize in the observed range. The lack of stability in the z-direction is due to the fact that this is the direction of stacking micrographs in the microstructure construction process. The dimension in this direction is therefore much less than the x- and y-directions, which leads to a reduced observation range. For all particles considered, the correlation lengths at different strains are similar. The lengths in the x-direction are slightly larger than those in y- and z-directions, revealing the effect of the extrusion direction on the characteristic length. Correlation lengths for the 20BL and 10BS materials are considerably lower than those for the 10BL material. However for cracked particles, the lengths for 10BL are less than those for 10BS but larger than those for 20BL composites. In this case, the correlation lengths are initially considerably higher, but decrease with subsequent deformation and particle cracking. It may therefore be projected, that the correlation length for the conjugate or uncracked particles will increase with deformation. Larger microstructural regions will thus be needed to constitute the RME with evolving damage.

6.2. Marked correlation function and characteristic length

Pyrz [38] has introduced the marked correlation function for multivariate characterization of patterns by associating field variables e.g. stresses within each particle in a heterogeneous domain. A mark may be identified with an appropriate microstructural variables to provide a criterion for determination of characteristic length scales [38,28,35]. The marked correlation function for a heterogeneous domain W of volume V containing N heterogeneities is mathematically expressed as [38,28]:

$$M(r) = \frac{\left[\dfrac{\mathrm{d}H(r)}{\mathrm{d}r}\right] \Big/ (4\pi r^2)}{g(r)} \tag{10}$$

where:

$$H(r) = \frac{1}{m^2}\frac{V}{N^2}\sum_{i=1}^{N}\sum_{k=1}^{k^i} m_i m_k(r),$$

$$g(r) = \frac{1}{4\pi r^2}\frac{\mathrm{d}K(r)}{\mathrm{d}r} \quad \text{and} \quad K(r) = \frac{V}{N^2}\sum_{k=1}^{N}\frac{I_k(r)}{R_\mathrm{p}}$$

$K(r)$ is the second order intensity function defined in [34,35], $g(r)$ is the pair distribution function and $H(r)$ is the mark intensity function. A mark associated with the ith heterogeneity is denoted as m_i, k^i is the number of heterogeneities which have their centers within a sphere of radius r around ith heterogeneity, for which the mark is m_k, and m is the mean of all marks. The marks considered in this study correspond to particle cracks and are designated as $m_i = 1$ for a cracked particle and $m_i = 2$ for an intact particle. Plots of $M(r)$ for various materials are illustrated in Fig. 12. The solid line corresponds to the unit $M(r)$ for uniform distribution of spherical heterogeneities with identical marks. The $M(r)$ function statistically stabilizes at near-unit values at a distance r_inter at which the local morphology ceases

Table 6
Comparison of Weibull model predicted and experimentally observed fraction of cracked particles

m	Without shape (Eq. (7))			With shape (Eq. (8))		
	10BL 9%	20BL 9%	10BS 6%	10BL 9%	20BL 6%	10BS 6%
1	0.1094	0.1159	0.1020	0.0751	0.0615	0.016409
2	0.1189	0.1303	0.1020	0.0838	0.0719	0.016408
3	0.1290	0.1460	0.1020	0.9346	0.0841	0.016413
4	0.1400	0.1629	0.1022	0.1042	0.0982	0.016400
5	0.1513	0.1807	0.1022	0.1164	0.1150	0.016424
6	0.1624	0.1985	0.10169	0.1299	0.1345	0.016358
7	0.1755	0.2186	0.1021	0.1449	0.1571	0.016325
8	0.1878	0.2379	0.10171	0.1611	0.1831	0.016387
Measured	0.1533	0.2187	0.0421	0.1533	0.2187	0.0421

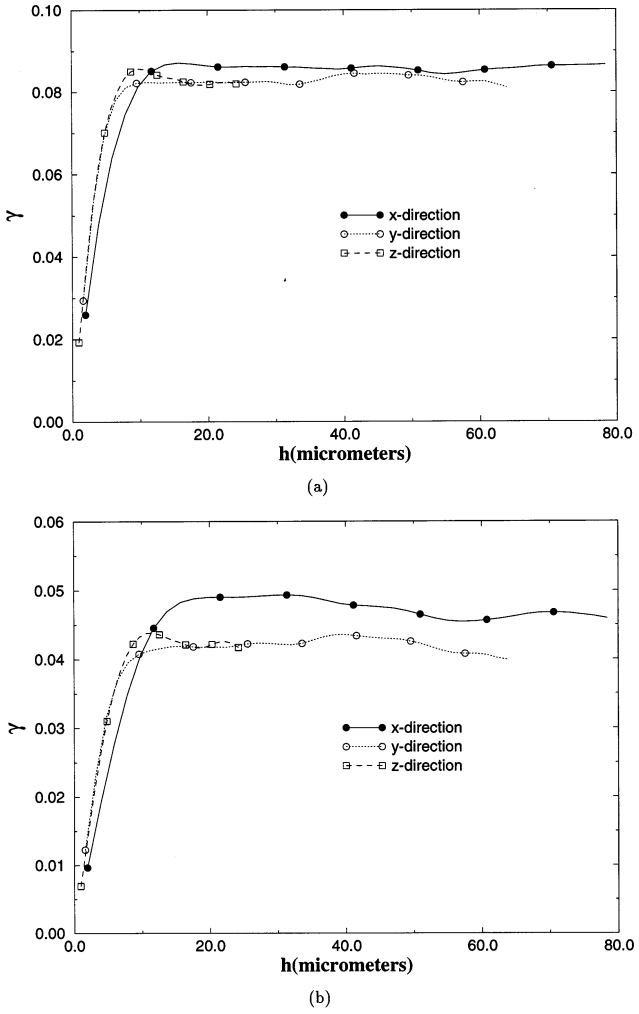

Fig. 11. Variograms of 10BL composite at 9% strain quantifying its fabric for (a) all particles and (b) cracked particles.

to have any significant influence on evolving variable. This distance r_{inter} provides an estimate on length scales related to the size of the RME. For the 10BL and 20BL materials in Fig. 12b and c it is seen that r_{inter} are approximately $13 \sim 16$ and 12 μm, respectively. These concur with the correlation lengths obtained from the variograms. $M(r)$ in Fig. 12a does not stabilize.

7. Discussion and conclusions

This is perhaps the first study to perform 3-D physical characterization of the damage structure for particle reinforced aluminum matrix composite materials. It presents a systematic approach to the characterization and modeling of damage with respect to phase morphology, for Si particle reinforced Al–Si–Mg matrix composites. As in the first paper [33] of this sequence, 3-D microstructures are computationally constructed from a series of parallel section micrographs which are generated by serial sectioning [33,30]. This results in a fairly high resolution with respect to particle and crack size and spacing. Equivalent microstructures with ellipsoidal particles and cracks are computationally simulated and are subsequently tessellated into Voronoi cells, based on particles or cracks.

Damage characterization with respect to microstructural morphology and deformation levels is conducted for both 2- and 3-D sections of materials with different volume fractions and particle sizes. Important microstructural features like size, local volume fraction, near-neighbor spacing and their clustering, that define the microstructural 'triggers' for damage evolution and dominant shear band and crack nucleation, are investigated. The morphological parameters which may be related to the damage process are selected as particle/crack size, shape and principal dimensions, relative distances and orientations, multiple cracks etc. In the image analysis process, statistical functions like mean and standard deviations, cumulative distribution and probability density functions of these parameters are evaluated. From the mean statistics, it is seen that the extent of damage, i.e. mean crack size and length, increase with deformation and particle size. The strain level and total volume fraction also enhance the chances of multiple cracks in particles. The mean damage size and major length decrease with deformation from an initial high, illustrating that the largest particles crack first. The minor dimension corresponding to the crack opening size, on the other hand, increases with deformation due widening. This also causes the mean aspect ratio to drop. The mean crack size is smaller in smaller particles (10BS) but increases with diminishing total volume fraction (20–10%). Particle cracking is found to have a strong correlation with the

Table 7
Correlation lengths for Al–Mg–Si composites in μm

Material	Strain (%)	All particles			Cracked particles		
10BL	6	16.2	13.9	15.2	23.0	18.4	15.4
10BL	9	16.4	10.8	14.9	18.8	12.6	11.1
10BS	6	8.6	6.5	8.1	51.3	41.6	–
20BL	6	11.6	8.5	–	13.6	12.6	–

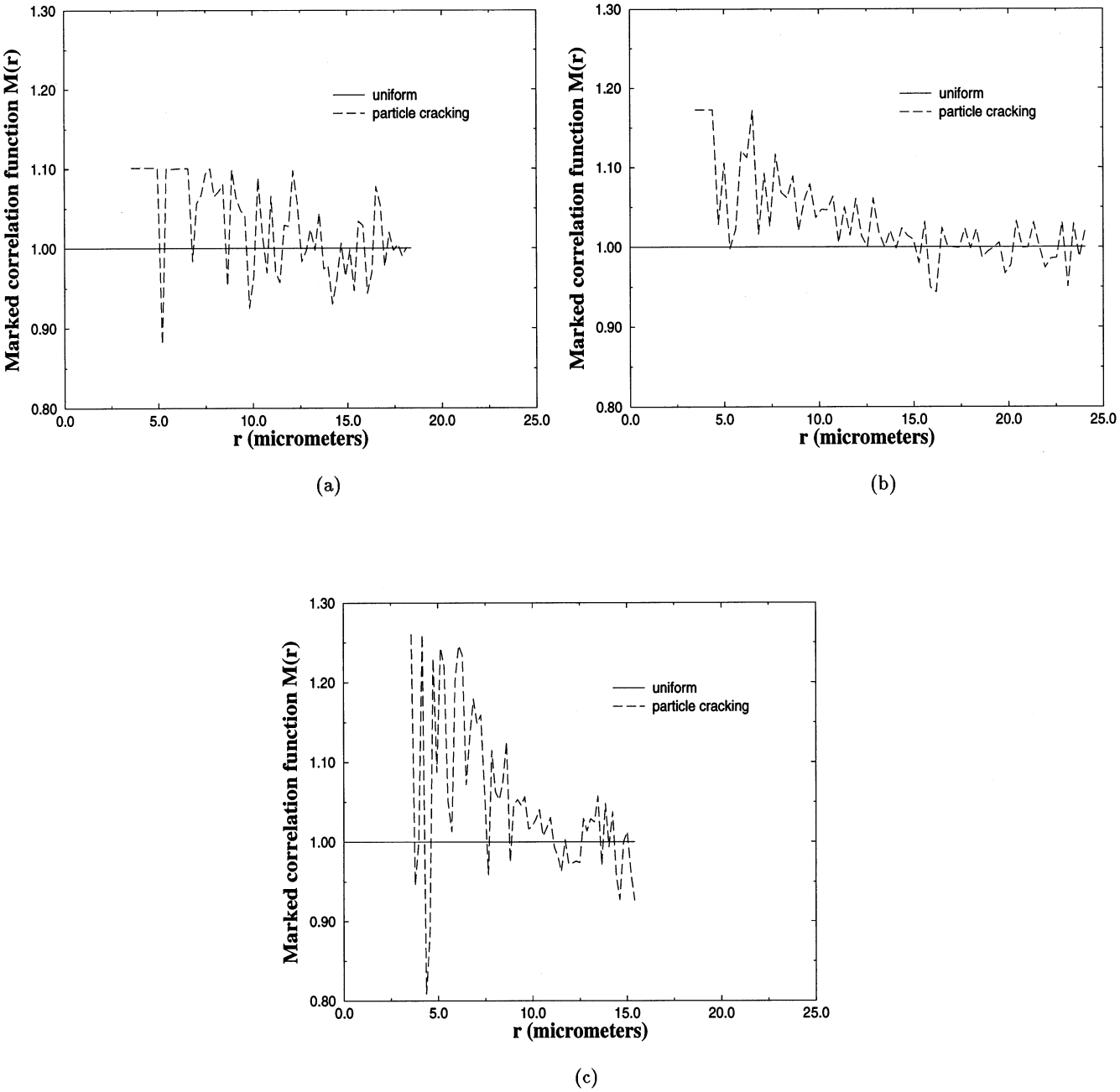

Fig. 12. Marked correlation functions for particle cracks (a) 10BL at 6% strain; (b) 10BL at 9% strain, and; (c) 20BL at 6% strain.

largest transverse cross-sectional area perpendicular to the loading direction. Particles with larger transverse cross-sectional areas are likely be cracked first. However not all cracks occur at the largest section and not all particles are completely split. Large particles with high aspect ratio and orientations closer to the loading direction are most prone to multi-cracking. For all results, the damage level in 3-D is significantly higher than that even in 2-D sections, reflecting the fact that many sections in a cracked particle do not reveal the damage. This may be because of the relative orientation of the particle and crack and the sectioning plane, and also their shapes. Consequently, the direct use of 2-D sections to infer damage is limited.

For the purpose of motivating a damage model, sensitivity analysis is performed for gagging the influence of different morphological variables on the damage process. The study includes the NFCP and the VFCP as damage parameters. Particle size, orientation with respect to the loading direction and local volume fraction are found to have strong influence on damage initiation. The effect of particle size is even more pronounced with evolving deformation. In comparison, particle shape and nearest neighbor distance have con-

siderably less effect. Interesting observations are made in the study of the straining effect on primary and secondary dimensions of particle cracks. While the rate of growth of the primary crack length tapers off after an initial high, that for the secondary length is steady and considerably slower.

For formulating a damage model, the most important variables are thus concluded to be particle size and local volume fraction, together with strain level and material properties. Results of the experimental analysis and characterization are compared with predictions of a two parameter Weibull model based on weakest link statistics. The model parameters are first calibrated from experimental results for the 10BL composite at 6% deformation. The fraction of cracked particles in the 10BL composite at 9% strain, the 20BL composite at 6% strain and the 10BS composite at 6% strain are then predicted by the Weibull model and compared with experiments. It is inferred that since the Weibull model does not account for particle orientations and spatial distributions, it is not very effective in predicting the extent of damage when morphology plays an important role. It is also noted that incorporation of shape and size in an uncorrelated manner may not be appropriate.

The representative material element (RME) corresponds to the region in the microstructure which can be represented by local constitutive models. It plays an important role in determining length scales. The data obtained through serial sectioning enables the 3-D estimation of these RME's, which is much more realistic than those inferred from 2-D analyses. RME estimates are obtained through the use of variograms [62] and also by marked correlation functions [28,35]. Correlation lengths in variograms are estimated as stabilization distances. In the absence of damage, these lengths are found to increase with higher particle size and lower volume fraction, and are also dependent on the extrusion direction in the fabrication process. Additionally, the correlation lengths for uncracked particles also increase with deformation. Marked correlation functions with cracked/uncracked particles as marks also yield similar observations. In conclusion, the comprehensive study for 3-D microstructures in this paper, establishes a new set of tools and functions for understanding the relationship of microstructural parameters to the initiation and evolution of damage.

Acknowledgements

The authors would like to thank Warren H. Hunt for offering the materials. The help of Byrl J. Johnson, Sally A. Jankosky, Rich Tallarico, D.H. Ringer, John C. Vilsack and W.R. Vogt of ALCOA Technical Center for help on image analysis, serial sectioning, specimen preparation and hardness measurement is highly appreciated. The first two authors have been supported by the Unites States Army Research Office through grant No. DAAH04-95-1-0176 (Program Director: Dr K.R. Iyer), by the National Science Foundation through a NSF Young Investigator grant (Grant No. CMS-9457603), by the Air Force Office of Scientific Research Office through grant No. F49620-98-1-01-93 (Program Director: Dr O.O. Ochoa), and by a grant from the ALCOA Technical Center. This sponsorship is gratefully acknowledged.

References

[1] P.M. Singh, J.J. Lewandowski, in: J.J. Lewandowski, W.H. Hunt (Eds.), Intrinsic and Extrinsic Fracture Mechanisms in Inorganic Composite Systems, Minerals, Metals and Materials Society, pp. 57.
[2] A. Vaidya, J.J. Lewandowski, in: J.J. Lewandowski, W.H. Hunt (Eds.), Intrinsic and Extrinsic Fracture Mechanisms in Inorganic Composite Systems, Minerals, Metals and Materials Society, 1995, pp. 147.
[3] J.J. Lewandowski, M. Manoharan, W.H. Hunt, Mater. Sci. Eng. A 172 (1993) 63.
[4] J.J. Lewandowski, P.M. Singh, in: J.J. Lewandowski, W.H. Hunt (Eds.), Intrinsic and Extrinsic Fracture Mechanisms in Inorganic Composite Systems, Minerals, Metals and Materials Society, 1995, pp. 129.
[5] J. Llorca, C. Gonzalaez, J. Mech. Phys. Solids 46 (1998) 1.
[6] A.B. Pandey, B.S. Majumdar, D.B. Miracle, Processing and fabrication of advanced materials, in: T.S. Srivatsan, J.J. Moore (Eds.), Proceedings of the TMS Conference, 1995, pp. 185.
[7] P.M. Mummery, B. Derby, C.B. Scruby, Acta Metall. Mater. 41 (1993) 1431.
[8] Y. Brechet, J.D. Embury, S. Tao, L. Luo, Acta Metall. Mater. 39 (1993) 1781.
[9] B.Y. Zong, B. Derby, J. Mater. Sci. 31 (1996) 297.
[10] P.M. Singh, J.J. Lewandowski, Metall. Trans. A 24A (1993) 2531.
[11] P.M. Singh, J.J. Lewandowski, Metall. Trans. A 26A (1995) 2911.
[12] P.M. Singh, J.J. Lewandowski, Scripta Metall. 29 (1993) 199.
[13] W.H. Hunt Jr., J.R. Brockenbrough, P.E. Magnusen, Scripta Metall. 25 (1991) 15.
[14] W.H. Hunt Jr., Microstructural Damage Processes in an Aluminum Matrix-silicon Particle Composite Model System, Ph.D. Thesis, Carnegie Mellon University, Pittsburgh, USA, 1992.
[15] J.J. Lewandowski, C. Liu, W.H. Hunt, Mater. Sci. Eng. A 107 (1989) 241.
[16] C. Liu, S. Pape, J.J. Lewandowski, in: H. Ishida (Ed.), Proceedings of the ICCI-II, Elsevier, New York, 1988, pp. 513.
[17] J.J. Lewandowski, C. Liu, in: D. Willkinson (Ed.), Proceedings of the Metals Society of the Canadian Institute for Mining and Metallurgy, vol. 2, Pergamon Press, 1988, pp. 23.
[18] J.J. Lewandowski, C. Liu, W.H. Hunt, Jr., Powder metallurgy composites, in: P. Kumar, K.M. Vedula, A.M. Ritter (Eds.), TMS-AIME, Warrendale, PA, pp. 117.
[19] J. Llorca, M. Elices, in: J.J. Lewandowski, W.H. Hunt (Eds.), Intrinsic and Extrinsic Fracture Mechanisms in Inorganic Composite Systems, Minerals, Metals and Materials Society, 1995, pp. 15.
[20] E. Maire, C. Verdu, G. Lormand, R. Fougeres, Mater. Sci. Eng. A 196 (1995) 135.

[21] C. Li, F. Ellyin, Mater. Sci. Eng. A 214 (1996) 115.
[22] C. Gonzalez, J. Llorca, Scripta Mater. 35 (1996) 91.
[23] F. Hild, in: D. Breysse (Ed.), Probabilities and Materials Tests, Models and Applications, Kluwer, Netherlands, 1994, pp. 427.
[24] D.J. Lloyd, Intrinsic and Extrinsic Fracture Mechanisms in Inorganic Composite Systems in: J.J. Lewandowski, W.H. Hunt (Eds.), Minerals, Metals and Materials Society, 1995, pp. 39.
[25] B.S. Majumdar, A.B. Pandey, Metall. Mater. Trans. (submitted for publication).
[26] C.W. Nan, D.R. Clarke, Acta Mater. 44 (1996) 3801.
[27] S. Moorthy, S. Ghosh, Comp. Meth. Appl. Mech. Eng. 151 (1998) 377.
[28] S. Ghosh, S. Moorthy, Acta Mater. 46 (1998) 965.
[29] R. Pyrz, B. Bochenek, Sci. Eng. Comp. Mat. 3 (1994) 95.
[30] M. Li, S. Ghosh, T.N. Rouns, H. Weiland, O. Richmond, W. Hunt, Mater. Charact. 41 (1998) 81.
[31] D.J. Lloyd, Acta Metall. Mater. 39 (1991) 59.
[32] J.D. Embury, F. Zok, D.J. Lahaie, W. Poole, in: J.J. Lewandowski, W.H. Hunt (Eds.), Intrinsic and Extrinsic Fracture Mechanisms in Inorganic Composite Systems, Minerals, Metals and Materials Society, 1995, pp. 1.
[33] M. Li, S. Ghosh, O. Richmond, H. Weiland, T.N. Rouns, Mater. Sci. Eng. (submitted for publication).
[34] S. Ghosh, Z. Nowak, K. Lee, Acta. Mater. 45 (1997) 2215.
[35] S. Ghosh, Z. Nowak, K. Lee, Comp. Sci. Tech. 57 (1997) 1187.
[36] W.A. Spitzig, J.F. Kelly, O. Richmond, Metallography 18 (1985) 235.
[37] P.J. Wray, O. Richmond, H.L. Morrison, Metallography 16 (1983) 39.
[38] R. Pyrz, Mater. Sci. Eng. A 177 (1994) 253.
[39] T.N. Rouns, J.M. Fridy, K.B. Lippert, O. Richmond, in: M.P. Anderson, A.D. Rollet (Eds.), Simulation and Theory of Evolving Microstructures, The Minerals and Materials Society, Warrendale, Pennsylvania, USA, 1990, pp. 269.
[40] J.M. Fridy, K. Marthinsen, T.N. Rouns, K.B. Lippert, E. Nes, O. Richmond, Proceedings of the 3rd International Conference on Aluminium Alloys, Trondheim, Norway, 1992, vol. 2, pp. 333.
[41] E.R. Weibel, Stereological Methods: Theoretical Foundation, vol. 2, Academic Press, London, 1980.
[42] L.M. Cruz-Orive, J. Microsc. 145 (1987) 121.
[43] S.K. Burke, S.McK. Cousland, C.M. Scala, Mater. Forum 18 (1994) 85.
[44] R.N. Yancey, G.Y. Baaklini, Proceedings of the ASME International Gas Turbine and Aeroengines Congress, Cincinnati, Ohio, USA, May 24–27, 1993.
[45] J.Y. Buffiere, E. Maire, C. Verdu, et al., Mater. Sci. Eng. A 234–236 (1997) 633.
[46] S.I. Rokhlin, W. Huang, Y.C. Chu, Ultrasonics 33 (1995) 351.
[47] P.T. Maclellan, Mater. Eval. 50 (1992) 1148.
[48] B.Derby, P.M.Mummery, C.W.Lawrence, in: J.J. Lewandowski, W.H. Hunt (Eds.), Intrinsic and Extrinsic Fracture Mechanisms in Inorganic Composite Systems, Minerals, Metals and Materials Society, 1995, pp. 7.
[49] S.T. Kim, Y.T. Lee, Mater. Sci. Eng. A 234–236 (1997) 322.
[50] P. Potet, C. Bathias, B. Degriguy, Mater. Eval. 46 (1988) 1050.
[51] B. London, R.N. Yancey, J.A. Smith, Mater. Eval. 48 (1990) 604.
[52] H. Weiland, T.N. Rouns, J. Liu, Z. Metallkd 85 (1994) 592.
[53] J. Llorca, Acta Metall. Mater. 43 (1995) 181.
[54] G. Bao, Acta Metall. Mater. 40 (1992) 2547.
[55] T. Christman, A. Needleman, S. Suresh, Acta Metall. Mater. 37 (1989) 3029.
[56] J.R. Brockenbrough, W.H. Hunt, O. Richmond, Scripta Metall. 27 (1992) 385.
[57] J.R. Brockenbrough, F.W. Zok, Acta Metall. Mater. 43 (1995) 11.
[58] L.C. Davis, J.E. Allison, Metal. Mater. Trans. A 26A (1995) 3081.
[59] L.C. Davis, C. Andres, J.E. Allison, Mater. Sci. Eng. A A249 (1998) 40.
[60] ABAQUS/Standard User's Manual, version 5.4, Hibbitt, Karlsson and Sorensen, Pawtucket, 1994, RI 02860–4847.
[61] M.T. Kiser, F.W. Zok, D.S. Wilkinsom, Acta Metall. Mater. 44 (1996) 3465.
[62] D. Breysse, P. Renaudin, European Workshop on Application of Statistics and Probability in Wood Mechanics, Bordeaux, Feb. 22–23, 1997.